JOURNAL OF COMPUTATIONAL PHYSICS **127,** 363–379 (1996)
ARTICLE NO. 0181

Three-Dimensional Perfectly Matched Layer for the Absorption of Electromagnetic Waves

JEAN-PIERRE BERENGER

Centre d'Analyse de Défense, 16 bis, Avenue Prieur de la Côte d'Or, 94114 Arcueil, France

Received March 13, 1995; revised October 12, 1995

The perfectly matched layer is a technique of free-space simulation developed for solving unbounded electromagnetic problems with the finite-difference time-domain method. Referred to as PML, this technique has been described in a previous paper for two-dimensional problems. The present paper is devoted to the three-dimensional case. The theory of the perfectly matched layer is generalized to three dimensions and some numerical experiments are shown to illustrate the efficiency of this new method of free-space simulation.

1. INTRODUCTION

The perfectly matched layer [1] is a new technique of free-space simulation developed for solving unbounded problems with the finite-difference time-domain method [2, 3]. Referred to as PML, this technique is based on the use of a layer especially designed to absorb the electromagnetic waves without reflection from the vacuum–layer interfaces. In [1] the layer and the free-space simulation technique were presented for two-dimensional problems. The present paper is devoted to the three-dimensional case.

The first part of the paper generalizes to three dimensions the theory of the PML medium [1]. It is shown that the theoretical properties of the 2D medium are preserved with the 3D one. The PML medium is then applied to build an absorbing layer to simulate free space on the outer boundary of a 3D computational domain. The second part of the paper is devoted to numerical experiments. Comparisons with two previously used techniques of free-space simulation are provided. These experiments show that the 3D PML method is very efficient and allows the absorption of the electromagnetic waves to be widely improved.

2. THEORY OF THE 3D PERFECTLY MATCHED LAYER

2.1. Definition of the PML Medium

In the PML medium, each component of the electromagnetic field is split into two parts. In cartesian coordinates, the six components yield 12 subcomponents denoted as E_{xy}, E_{xz}, E_{yz}, E_{yx}, E_{zx}, E_{zy}, H_{xy}, H_{xz}, H_{yz}, H_{yx}, H_{zx}, H_{zy}, and the Maxwell equations are replaced by 12 equations,

$$\varepsilon \frac{\partial E_{xy}}{\partial t} + \sigma_y E_{xy} = \frac{\partial (H_{zx} + H_{zy})}{\partial y} \tag{1.a}$$

$$\varepsilon \frac{\partial E_{xz}}{\partial t} + \sigma_z E_{xz} = -\frac{\partial (H_{yz} + H_{yx})}{\partial z} \tag{1.b}$$

$$\varepsilon \frac{\partial E_{yz}}{\partial t} + \sigma_z E_{yz} = \frac{\partial (H_{xy} + H_{xz})}{\partial z} \tag{1.c}$$

$$\varepsilon \frac{\partial E_{yx}}{\partial t} + \sigma_x E_{yx} = -\frac{\partial (H_{zx} + H_{zy})}{\partial x} \tag{1.d}$$

$$\varepsilon \frac{\partial E_{zx}}{\partial t} + \sigma_x E_{zx} = \frac{\partial (H_{yz} + H_{yx})}{\partial x} \tag{1.e}$$

$$\varepsilon \frac{\partial E_{zy}}{\partial t} + \sigma_y E_{zy} = -\frac{\partial (H_{xy} + H_{xz})}{\partial y} \tag{1.f}$$

$$\mu \frac{\partial H_{xy}}{\partial t} + \sigma_y^* H_{xy} = -\frac{\partial (E_{zx} + E_{zy})}{\partial y} \tag{1.g}$$

$$\mu \frac{\partial H_{xz}}{\partial t} + \sigma_z^* H_{xz} = \frac{\partial (E_{yz} + E_{yx})}{\partial z} \tag{1.h}$$

$$\mu \frac{\partial H_{yz}}{\partial t} + \sigma_z^* H_{yz} = -\frac{\partial (E_{xy} + E_{xz})}{\partial z} \tag{1.i}$$

$$\mu \frac{\partial H_{yx}}{\partial t} + \sigma_x^* H_{yx} = \frac{\partial (E_{zx} + E_{zy})}{\partial x} \tag{1.j}$$

$$\mu \frac{\partial H_{zx}}{\partial t} + \sigma_x^* H_{zx} = -\frac{\partial (E_{yz} + E_{yx})}{\partial x} \tag{1.k}$$

$$\mu \frac{\partial H_{zy}}{\partial t} + \sigma_y^* H_{zy} = \frac{\partial (E_{xy} + E_{xz})}{\partial y}, \tag{1.l}$$

where the parameters $(\sigma_x, \sigma_y, \sigma_z, \sigma_x^*, \sigma_y^*, \sigma_z^*)$ are homogeneous to electric and magnetic conductivities.

0021-9991/96 $18.00

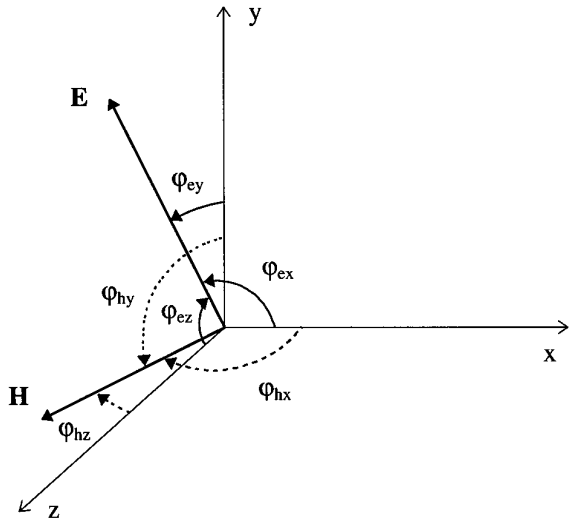

FIG. 1. Propagation of a plane wave in a PML medium.

If both $\sigma_x = \sigma_y = \sigma_z$ and $\sigma_x^* = \sigma_y^* = \sigma_z^* = 0$ we can note that (1) yields the Maxwell equations. Thus, the absorbing medium defined by (1) holds as particular cases all the usual media (vacuum, conductive media). In the 2D cases [1], due to the symmetry of the problem, (1) reduces to a set of four equations. Only one component is split into two subcomponents, either the magnetic component in the TE case or the electric component in the TM case.

2.2. Propagation of a Plane Wave in a PML Medium

Let us consider a propagating plane wave whose electric and magnetic fields form the angles φ_{ex}, φ_{ey}, φ_{ez} and φ_{hx}, φ_{hy}, φ_{hz} with the coordinate axis (Fig. 1). Let E_0, H_0 be their magnitudes and let E_{xy0}, E_{xz0}, E_{yz0}, ..., H_{zx0}, H_{zy0} be the magnitudes of the 12 subcomponents. If this wave propagates in the PML medium, the 12 subcomponents can be written as

$$E_{xy} = E_{xy0} e^{i\omega(t-\alpha x-\beta y-\gamma z)} \tag{2.a}$$

$$E_{xz} = E_{xz0} e^{i\omega(t-\alpha x-\beta y-\gamma z)} \tag{2.b}$$

$$\cdots \qquad \cdots$$

$$H_{zx} = H_{zx0} e^{i\omega(t-\alpha x-\beta y-\gamma z)} \tag{2.k}$$

$$H_{zy} = H_{zy0} e^{i\omega(t-\alpha x-\beta y-\gamma z)}. \tag{2.l}$$

Inserting (2) into (1) yields the 12 equations

$$\varepsilon S_y E_{xy0} = -\beta H_0 \cos\varphi_{hz} \tag{3.a}$$

$$\varepsilon S_z (E_0 \cos\varphi_{ex} - E_{xy0}) = \gamma H_0 \cos\varphi_{hy} \tag{3.b}$$

$$\cdots \qquad \cdots$$

$$\mu S_x^* H_{zx0} = \alpha E_0 \cos\varphi_{ey} \tag{3.k}$$

$$\mu S_y^* (H_0 \cos\varphi_{hz} - H_{zx0}) = -\beta E_0 \cos\varphi_{ex}, \tag{3.l}$$

where

$$S_u = 1 - i\frac{\sigma_u}{\varepsilon\omega}, \quad S_u^* = 1 - i\frac{\sigma_u^*}{\mu\omega} \quad (u = x, y, z). \tag{4}$$

Inserting E_{xy0} from (3.a) into (3.b), ..., and H_{zx0} from (3.k) into (3.l), we obtain a system of six equations in which Z is the ratio E_0/H_0:

$$\varepsilon Z \cos\varphi_{ex} = \frac{\gamma}{S_z}\cos\varphi_{hy} - \frac{\beta}{S_y}\cos\varphi_{hz} \tag{5.a}$$

$$\varepsilon Z \cos\varphi_{ey} = \frac{\alpha}{S_x}\cos\varphi_{hz} - \frac{\gamma}{S_z}\cos\varphi_{hx} \tag{5.b}$$

$$\varepsilon Z \cos\varphi_{ez} = \frac{\beta}{S_y}\cos\varphi_{hx} - \frac{\alpha}{S_x}\cos\varphi_{hy} \tag{5.c}$$

$$\mu\frac{1}{Z}\cos\varphi_{hx} = -\frac{\gamma}{S_z^*}\cos\varphi_{ey} + \frac{\beta}{S_y^*}\cos\varphi_{ez} \tag{5.d}$$

$$\mu\frac{1}{Z}\cos\varphi_{hy} = -\frac{\alpha}{S_x^*}\cos\varphi_{ez} + \frac{\gamma}{S_z^*}\cos\varphi_{ex} \tag{5.e}$$

$$\mu\frac{1}{Z}\cos\varphi_{hz} = -\frac{\beta}{S_y^*}\cos\varphi_{ex} + \frac{\alpha}{S_x^*}\cos\varphi_{ey}. \tag{5.f}$$

From (5), it is easy to show that

$$\cos\varphi_{ex}\cos\varphi_{hx} + \cos\varphi_{ey}\cos\varphi_{hy} + \cos\varphi_{ez}\cos\varphi_{hz} = 0 \tag{6}$$

$$\frac{\alpha}{S_x}\cos\varphi_{ex} + \frac{\beta}{S_y}\cos\varphi_{ey} + \frac{\gamma}{S_z}\cos\varphi_{ez} = 0 \tag{7.a}$$

$$\frac{\alpha}{S_x^*}\cos\varphi_{hx} + \frac{\beta}{S_y^*}\cos\varphi_{hy} + \frac{\gamma}{S_z^*}\cos\varphi_{hz} = 0 \tag{7.b}$$

$$\frac{\alpha^2}{S_x S_x^*} + \frac{\beta^2}{S_y S_y^*} + \frac{\gamma^2}{S_z S_z^*} = \varepsilon\mu \tag{7.c}$$

Equation (6) means that the electric and magnetic fields are perpendicular in a PML medium. From (2) we can write $\alpha = k_x/\omega$, $\beta = k_y/\omega$, and $\gamma = k_z/\omega$, so that (7.c) is the dispersion relation of the PML equations (1), connecting ω

to the wave numbers k_x, k_y, k_z. As expected, if $\sigma_x = \sigma_y = \sigma_z$ and $\sigma_x^* = \sigma_y^* = \sigma_z^* = 0$ this equation reduces to the dispersion relation of the Maxwell equations. Multiplying then (5.b) by $\cos \varphi_{hz}\ S_z/S_z^*$ and (5.c) by $\cos \varphi_{hy}\ S_y/S_y^*$, subtracting the resulting equations, and taking into account (7.b), one can show that

$$\alpha = \varepsilon S_x \frac{\dfrac{S_z}{S_z^*}\cos \varphi_{ey} \cos \varphi_{hz} - \dfrac{S_y}{S_y^*}\cos \varphi_{ez} \cos \varphi_{hy}}{\dfrac{S_x}{S_x^*}\cos^2 \varphi_{hx} + \dfrac{S_y}{S_y^*}\cos^2 \varphi_{hy} + \dfrac{S_z}{S_z^*}\cos^2 \varphi_{hz}} Z. \quad (8)$$

Similar formulas can be obtained for β and γ from (5), or from (8) by circular permutations of the coordinates. Inserting then α and β into (5.f) and taking into account (6), the impedance Z is

$$Z = \sqrt{\mu/\varepsilon}\,(1/G), \quad (9)$$

where

$$G = \sqrt{\frac{w_y w_z \cos^2 \varphi_{ex} + w_z w_x \cos^2 \varphi_{ey} + w_x w_y \cos^2 \varphi_{ez}}{w_x \cos^2 \varphi_{hx} + w_y \cos^2 \varphi_{hy} + w_z \cos^2 \varphi_{hz}}} \quad (10)$$

and

$$w_u = \frac{S_u}{S_u^*} = \frac{1 - i\sigma_u/\varepsilon\omega}{1 - i\sigma_u^*/\mu\omega} \quad (u = x, y, z). \quad (11)$$

From (8), (9), and (11), we have

$$\alpha = \frac{\sqrt{\varepsilon\mu}}{G} S_x \frac{w_z \cos \varphi_{ey} \cos \varphi_{hz} - w_y \cos \varphi_{ez} \cos \varphi_{hy}}{w_x \cos^2 \varphi_{hx} + w_y \cos^2 \varphi_{hy} + w_z \cos^2 \varphi_{hz}} \quad (12.a)$$

$$\beta = \frac{\sqrt{\varepsilon\mu}}{G} S_y \frac{w_x \cos \varphi_{ez} \cos \varphi_{hx} - w_z \cos \varphi_{ex} \cos \varphi_{hz}}{w_x \cos^2 \varphi_{hx} + w_y \cos^2 \varphi_{hy} + w_z \cos^2 \varphi_{hz}} \quad (12.b)$$

$$\gamma = \frac{\sqrt{\varepsilon\mu}}{G} S_z \frac{w_y \cos \varphi_{ex} \cos \varphi_{hy} - w_x \cos \varphi_{ey} \cos \varphi_{hx}}{w_x \cos^2 \varphi_{hx} + w_y \cos^2 \varphi_{hy} + w_z \cos^2 \varphi_{hz}}. \quad (12.c)$$

If the couples of conductivities (σ_x, σ_x^*), (σ_y, σ_y^*), (σ_z, σ_z^*), satisfy the usual matching impedance condition $(\sigma/\varepsilon = \sigma^*/\mu)$, we have $w_x = w_y = w_z = 1$ so that $G = 1$. Then, the impedance Z equals that of a medium (ε, μ). In this case, denoting by η_x, η_y, η_z the angles that the perpendicular to the (E, H) plane forms with the coordinate axis, in (12) the numerators in the ratios equal respectively $\cos \eta_x$, $\cos \eta_y$, $\cos \eta_z$, and the denominators equal one. As a result, from (2), (4), and (12), in such a matched PML medium, any subcomponent of the propagating wave (2) is of the following form, in which $c = (\varepsilon\ \mu)^{-1/2}$:

$$\Psi = \Psi_0\, e^{i\omega(t-(x\cos\eta_x + y\cos\eta_y + z\cos\eta_z)/c)}\, e^{-(\sigma_x \cos\eta_x/\varepsilon c)\,x}\, e^{-(\sigma_y \cos\eta_y/\varepsilon c)\,y}\, e^{-(\sigma_z \cos\eta_z/\varepsilon c)\,z}. \quad (13)$$

Thus, if the conductivities satisfy the matching impedance condition, the phase propagates perpendicularly to the (E, H) plane, as in a vacuum, and the magnitude of the wave is governed by the last three exponential terms. This formula is analogous to that of the two-dimensional case [1]. The coordinates x, y, z are embedded in separate absorbing terms, allowing the wave to be damped along one or two directions by selecting an adequate set of conductivities. If $\sigma_y = \sigma_z = 0$ a wave propagating perpendicularly to the x axis is not absorbed, as when $\sigma_y = 0$ in the 2D case. We can note that the 3D theory includes the 2D theory [1] as a special case. For instance, in the TE case: considering the angle φ defined in [1] we have $\varphi_{ex} = \varphi + \pi/2$, $\varphi_{ey} = \varphi$, $\varphi_{hz} = 0$, $\varphi_{ez} = \varphi_{hx} = \varphi_{hy} = \pi/2$, so that (10) and (12) give the corresponding equations of [1].

2.3. Transmission of a Wave through PML–PML Interfaces

We will consider two PML media separated by an interface perpendicular to the x axis (Fig. 2). In each media, let us denote by (θ_e, ϕ_e) and (θ_h, ϕ_h) the angles that the electric and magnetic fields form with the (y, z) plane and the y axis (Fig. 2). The angles φ_{ex}, ..., φ_{hz} defined in the previous section are related to the new angles by the following relations which are valid for both the electric and magnetic fields ($u = e$ or h):

$$\cos \varphi_{ux} = -\sin \theta_u \quad (14.a)$$

$$\cos \varphi_{uy} = \cos \theta_u \cos \phi_u \quad (14.b)$$

$$\cos \varphi_{uz} = \cos \theta_u \sin \phi_u. \quad (14.c)$$

Inserting (14) into (10) and (12) yields α, β, γ, G as functions of θ_e, ϕ_e, θ_h, ϕ_h. We now consider the transmission of two polarizations of an incident wave: first, the transverse electric polarization; second, the transverse magnetic polarization.

Transverse Electric Case TE

In this case, the magnetic field lies in a plane parallel to the interface. We have $\theta_h = 0$, $\phi_h = \phi_{e+}\pi/2$, since electric and magnetic fields are perpendicular from (6), and $\theta_e =$

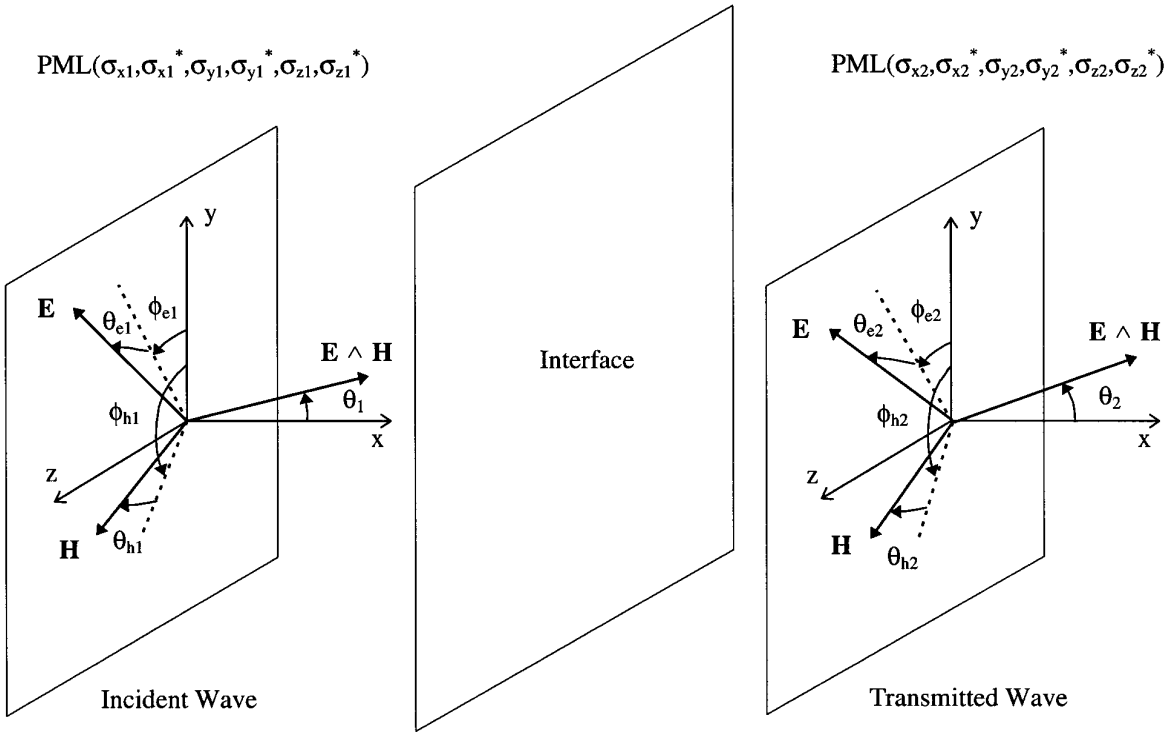

FIG. 2. Interface lying between two PML media.

θ where θ is the angle that the normal to the (E, H) plane forms with the normal to the interface. Inserting (14) into (10) and (12) yields

$$\beta = \frac{\sqrt{\varepsilon\mu}}{G} S_y \frac{w_z \sin\theta \sin\phi_h}{w_y \cos^2\phi_h + w_z \sin^2\phi_h} \tag{15.a}$$

$$\gamma = -\frac{\sqrt{\varepsilon\mu}}{G} S_z \frac{w_y \sin\theta \cos\phi_h}{w_y \cos^2\phi_h + w_z \sin^2\phi_h} \tag{15.b}$$

$$G = \sqrt{\frac{w_y w_z \sin^2\theta + w_z w_x \cos^2\theta \sin^2\phi_h + w_x w_y \cos^2\theta \cos^2\phi_h}{w_y \cos^2\phi_h + w_z \sin^2\phi_h}}. \tag{16}$$

At an interface between two media, the ratio of the transmitted wave to the incident wave must be invariable when moving in the interface. As a result, the same demonstration as that in [1] yields the Snell–Descartes law connecting the β_1 and γ_1 coefficients of the incident wave to the β_2 and γ_2 coefficients of the transmitted wave:

$$\beta_1 = \beta_2, \quad \gamma_1 = \gamma_2. \tag{17}$$

Using (15) in both media, the ratio of these two equations gives

$$\frac{S_{y1}^*}{S_{z1}^*} \tan\phi_{h1} = \frac{S_{y2}^*}{S_{z2}^*} \tan\phi_{h2}. \tag{18}$$

This relation shows that $\sin\phi_{h1} = \sin\phi_{h2}$ and $\cos\phi_{h1} = \cos\phi_{h2}$ in the following two cases:

—$\sigma_{y1}^* = \sigma_{z1}^*$ and $\sigma_{y2}^* = \sigma_{z2}^*$. If, moreover, $\sigma_{y1} = \sigma_{z1}$ and $\sigma_{y2} = \sigma_{z2}$, this case is two-dimensional. By rotating the (y, z) plane of coordinates, (15), (16), and (17) yield the TE results of [1].

—$\sigma_{y1}^* = \sigma_{y2}^*$ and $\sigma_{z1}^* = \sigma_{z2}^*$. The transverse magnetic conductivities of the two media are equal. This case is a true 3D case. Using (15), both Equations (17) become

$$\frac{\sqrt{\varepsilon_1\mu_1}\, S_{y1} S_{z1} \sin\theta_1}{w_{y1}\cos^2\phi_{h1} + w_{z1}\sin^2\phi_{h1}} \frac{1}{G_1} = \frac{\sqrt{\varepsilon_2\mu_2}\, S_{y2} S_{z2} \sin\theta_2}{w_{y2}\cos^2\phi_{h1} + w_{z2}\sin^2\phi_{h1}} \frac{1}{G_2}. \tag{19}$$

For the reflected wave, a similar demonstration yields the corresponding angle θ equal to $\pi - \theta_1$. Let us now consider the incident, reflected, and transmitted fields E_i, E_r, E_t, H_i, H_r, H_t. Continuity of the components in the interface gives

$$E_i \cos\theta_1 - E_r \cos\theta_1 = E_t \cos\theta_2 \tag{20.a}$$

$$H_i + H_r = H_t \tag{20.b}$$

These equations are identical to those of the 2D case and yield the same reflection coefficient r_p:

$$r_p = \frac{Z_2 \cos\theta_2 - Z_1 \cos\theta_1}{Z_2 \cos\theta_2 + Z_1 \cos\theta_1}. \tag{21}$$

We now consider two media having the same transverse conductivities, the same permittivity, and the same permeability, so that σ_y, σ_y^*, σ_z, σ_z^*, ε, μ of the two media are equal. From (19) we have

$$\frac{\sin\theta_1}{G_1} = \frac{\sin\theta_2}{G_2}. \tag{22}$$

If, moreover, the two media are matched ones, that is (σ_x, σ_x^*), (σ_y, σ_y^*), and (σ_z, σ_z^*), satisfying the condition $\sigma/\varepsilon = \sigma^*/\mu$ in each medium, we have $G_1 = G_2 = 1$, so that $\theta_1 = \theta_2$ from (22) and $Z_1 = Z_2$ from (9). As a result, (21) becomes

$$r_p = 0. \tag{23}$$

The TE component is not reflected from an interface normal to x lying between two matched media having the same σ_y, σ_y^*, σ_z, σ_z^* conductivities. This result generalizes the 2D case [1]. If ε and μ of the matched media are not equal, rewriting (22) from (19) shows that r_p is as an interface lying between the usual (ε_1, μ_1) and (ε_2, μ_2) media, provided $\sigma_{y2}/\sigma_{y1} = \sigma_{z2}/\sigma_{z1} = \varepsilon_2/\varepsilon_1$.

In the case of unmatched media having the same σ_y, σ_y^*, σ_z, σ_z^*, a simple formula can be obtained for the reflection coefficient, as in [1]. Using (9) and (22) the reflection coefficient (21) becomes

$$r_p = \frac{\sin\theta_1 \cos\theta_2 - \sin\theta_2 \cos\theta_1}{\sin\theta_1 \cos\theta_2 + \sin\theta_2 \cos\theta_1}. \tag{24}$$

Squaring (22), replacing G_1 and G_2 by their values from (16), we obtain

$$\sqrt{w_{x2}} \sin\theta_1 \cos\theta_2 = \sqrt{w_{x1}} \sin\theta_2 \cos\theta_1. \tag{25}$$

Formulas (24) and (25) are identical to those of the 2D case [1], and so they yield the same reflection coefficient for two unmatched media having the same transverse conductivities σ_y, σ_y^*, σ_z, σ_z^*:

$$r_p = \frac{\sqrt{w_{x1}} - \sqrt{w_{x2}}}{\sqrt{w_{x1}} + \sqrt{w_{x2}}}. \tag{26}$$

Transverse Magnetic Case TM

The electric field lies in a plane parallel to the interface. We have $\theta_e = 0$, $\phi_h = \phi_e + \pi/2$, and $\theta_h = \theta$. From (9), (10), and (12),

$$\beta = -\sqrt{\varepsilon\mu} G S_y \frac{\sin\theta \sin\phi_e}{w_z \cos^2\phi_e + w_y \sin^2\phi_e} \tag{27.a}$$

$$\gamma = \sqrt{\varepsilon\mu} G S_z \frac{\sin\theta \cos\phi_e}{w_z \cos^2\phi_e + w_y \sin^2\phi_e} \tag{27.b}$$

$$G = \sqrt{\frac{w_z w_x \cos^2\phi_e + w_x w_y \sin^2\phi_e}{w_x \sin^2\theta + w_y \cos^2\theta \sin^2\phi_e + w_z \cos^2\theta \cos^2\phi_e}}. \tag{28}$$

From (27) and (17) which is valid for any polarization,

$$\frac{S_{y1}}{S_{z1}} \tan\phi_{e1} = \frac{S_{y2}}{S_{z2}} \tan\phi_{e2}. \tag{29}$$

We have $\sin\phi_{e1} = \sin\phi_{e2}$ and $\cos\phi_{e1} = \cos\phi_{e2}$ in the following cases:

—$\sigma_{y1} = \sigma_{z1}$ and $\sigma_{y2} = \sigma_{z2}$. If, moreover, $\sigma_{y1}^* = \sigma_{z1}^*$ and $\sigma_{y2}^* = \sigma_{z2}^*$ this case yields the 2D TM case briefly described in [1].

—$\sigma_{y1} = \sigma_{y2}$ and $\sigma_{z1} = \sigma_{z2}$. This is a true 3D case. Using (27), Eqs. (17) become

$$\frac{\sqrt{\varepsilon_1\mu_1}\, G_1 \sin\theta_1}{w_{z1} \cos^2\phi_{e1} + w_{y1} \sin^2\phi_{e1}} = \frac{\sqrt{\varepsilon_2\mu_2}\, G_2 \sin\theta_2}{w_{z2} \cos^2\phi_{e1} + w_{y2} \sin^2\phi_{e1}}. \tag{30}$$

As in the TE case, continuity of the components lying in the interface yields the usual r_s reflection coefficient,

$$r_s = \frac{Z_2 \cos\theta_1 - Z_1 \cos\theta_2}{Z_2 \cos\theta_1 + Z_1 \cos\theta_2}. \tag{31}$$

If the media have the same transverse conductivities σ_y, σ_y^*, σ_z, σ_z^*, the same permittivity ε, and the same permeability μ, (30) becomes

$$G_1 \sin\theta_1 = G_2 \sin\theta_2. \tag{32}$$

If, moreover, the two media are matched ones, $G_1 = G_2 = 1$, $\theta_1 = \theta_2$, $Z_1 = Z_2$, so that

$$r_s = 0. \tag{33}$$

The TM components are not reflected from an interface normal to the x axis lying between two matched media having the same transverse conductivities σ_y, σ_y^*, σ_z, σ_z^*.

In the case of two unmatched media of the same transverse conductivities, it can be shown that (26) also holds for the TM coefficient r_s. Using (9) and(32) one can obtain r_s equal to the opposite sign of (24). Squaring (32) yields (25) with w_{x1} and w_{x2} interchanged. The modified equations (24) and (25) give then r_s equal to the r_p coefficient (26).

Summary and Conclusions

Any plane wave can be split into TE and TM polarizations. Thus, for any propagating plane wave we have the following theoretical properties at an interface normal to x lying between PML media of same ε and μ:

—if the transverse conductivities σ_y, σ_y^*, σ_z, σ_z^* are equal, the reflection is given by (26).

—if, moreover, all couples of conductivities satisfy the matching impedance condition in both media, there is no reflection at any angle of incidence and any frequency.

Obviously these properties are also valid at interfaces normal to y and normal to z, the transverse conductivities being respectively σ_z, σ_z^*, σ_x, σ_x^* and σ_x, σ_x^*, σ_y, σ_y^*.

An important case occurs when one medium is a vacuum, or a medium of real ε and μ. Since a vacuum can be regarded as a (0, 0, 0, 0, 0, 0) PML medium, there is no reflection from an interface located between a vacuum and a PML medium whose transverse conductivities equal zero and whose longitudinal conductivities satisfy the matching condition. For instance, the reflection equals zero from an interface normal to y located between a vacuum and a (0, 0, σ_y, σ_y^*, 0, 0) medium, provided $\sigma_y/\varepsilon_0 = \sigma_y^*/\mu_0$. Such a special case will be used in the PML technique to ensure zero reflection from the vacuum–layer interfaces. Actually, as remarked before, this case is 2D and the demonstration in [1] ensures zero reflection. In the implementation of the PML technique, the 3D theory will only be called for the small interfaces located inside the PML layer near the edges and the corners (see the next section).

In conclusion, the properties of the 2D PML medium [1] are preserved in the 3D case. This will allow an absorbing layer to be built on the outer boundary of a computational domain, without theoretical reflection of plane waves from vacuum–layer interfaces. As in [1], only propagating waves were considered above, nevertheless such an absence of reflection from interfaces is also true with evanescent waves (see the Conclusion).

As a final remark, in the definition of the PML medium (1), electric and magnetic fields are symmetrical. The result is that a dual formulation can be derived from (5). In dual formulas, with G changed to $1/G$ in its definition (9), the sign of (12) is changed and φ_e, φ_h, S, w are replaced by φ_h, φ_e, S^*, $1/w$ in (10) and (12). The TE and TM cases are interchanged, the duals of (15) and (16) being (27) and (28) with ϕ_e, w, replaced by ϕ_h, $1/w$ and an opposite sign in (27), and vice versa for the duals of (27) and (28).

2.4. Perfectly Matched Layer for the Finite Difference Technique

The 3D PML technique is a straightforward generalization of the 2D one presented in [1]. The Maxwell equations are solved by the FDTD method [2, 3] within a computational domain surrounded by an absorbing layer which is an aggregate of PML media whose properties have been predicted in previous sections.

In the six sides of the domain, the absorbing media are matched PML media of transverse conductivities equal to zero, for instance, (0, 0, 0, 0, σ_z, σ_z^*) media in the upper and lower sides of the domain (Fig. 3). As a result, outgoing waves from the inner vacuum can penetrate without reflection into these absorbing layers.

In the 12 edges, the conductivities are selected in such a way that the transverse conductivities are equal at the interfaces located between edge media and side media. This is obtained by means of two conductivities equal to zero and the other four equal to the conductivities of the adjacent side media, as shown in Fig. 3. As a result, there is theoretically no reflection from the side–edge interfaces.

In the eight corners of the domain, the conductivities are chosen equal to those of the adjacent edges, so that the transverse conductivities are equal at the interfaces between edge layers and corner layers. So, the reflection equals zero from all the edge–corner interfaces.

Thus, as in the 2D cases [1], in the 3D case an absorbing layer can be built in such a way that there is no theoretical reflection from any of the interfaces in the computational domain.

Numerical implementation of the PML layer in a 3D FDTD domain is also a straightforward generalization of the 2D case [1]. In the inner vacuum, the finite-difference equations are the usual [2, 3] discretizations of the Maxwell equations. In the PML layer, there are 12 subcomponents to be computed in place of the six components. The Yee

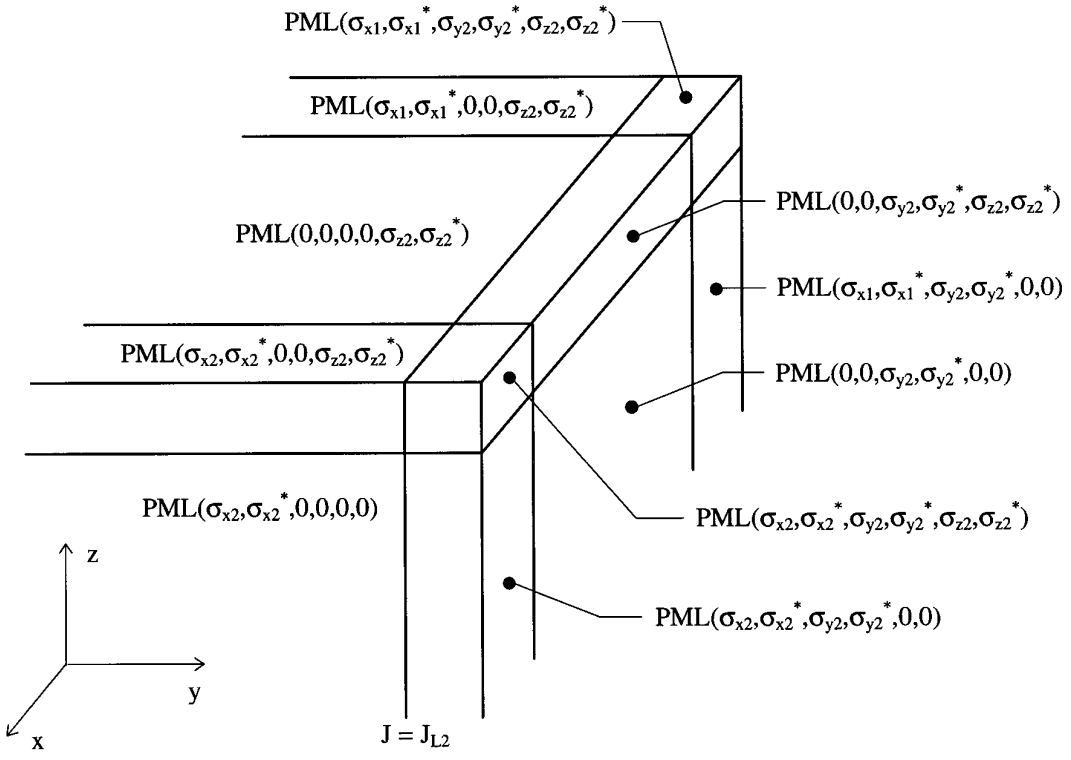

FIG. 3. Upper-right part of a computational domain surrounded by the PML layer.

FDTD grid is unchanged, the only change is that two subcomponents are computed at each point of the grid, E_{xy} and E_{xz} at E_x points, . . ., H_{zx} and H_{zy} at H_z points. Discretization of (1) is obvious, as in 2D. For instance, with the usual notations of the FDTD scheme, E_{xy} is computed by the equation derived from (1.a),

$$\begin{aligned} E_{xy}^{n+1}(i+\tfrac{1}{2},j,k) &= e^{-\sigma_y(i+1/2,j,k)\Delta t/\varepsilon} E_{xy}^{n}(i+\tfrac{1}{2},j,k) \\ &+ \frac{1-e^{-\sigma_y(i+1/2,j,k)\Delta t/\varepsilon}}{\sigma_y(i+\tfrac{1}{2},j,k)\Delta y} \\ &\times [H_{zx}^{n+1/2}(i+\tfrac{1}{2},j+\tfrac{1}{2},k) \\ &+ H_{zy}^{n+1/2}(i+\tfrac{1}{2},j+\tfrac{1}{2},k) \\ &- H_{zx}^{n+1/2}(i+\tfrac{1}{2},j-\tfrac{1}{2},k) \\ &- H_{zy}^{n+1/2}(i+\tfrac{1}{2},j-\tfrac{1}{2},k)], \end{aligned} \tag{34}$$

where σ_y depends on the location in the layer. With interfaces normal to y located at index J_{L1} and J_{L2} as in Fig. 3, $\sigma_y = \sigma_{y1}$ if $J \le J_{L1}$, $\sigma_y = 0$ if $J_{L1} < J < J_{L2}$, and $\sigma_y = \sigma_{y2}$ if $J \ge J_{L2}$.

For computing the tangential subcomponents in the vacuum–layer interfaces, as E_{yx} and E_{zx} in the interfaces normal to x, the numerical derivatives involve one point in the vacuum and the other in the PML layer. Such derivatives are obtained by using the component in the vacuum and the sum of the two subcomponents in the layer, as detailed for the 2D case in [1].

Continuity of tangential components at vacuum-layer interfaces is ensured as with the Maxwell equations, by the normal derivatives computed using one point in the vacuum and one point in the layer. Such a continuity in the numerical implementation is consistent with the theoretical continuity enforced in (20), and then with the reflection coefficients (23) and (33).

The theoretical properties of the PML layers were demonstrated above for continuous media. From this ideal point of view, there is no reflection from all the interfaces in the computational domain. Unfortunately, that is not the case in the FDTD implementation of the PML technique. Due to the discretization of the PML equations, a certain amount of numerical reflection occurs from sharp variations of conductivities at the interfaces. As in the 2D case [1], in order to reduce this reflection the conductivities σ_x, σ_y, σ_z increase from a small value in the vacuum–layer interfaces to a great value on the outer boundaries. This means that the conductivity in side layers depends on the distance from the interface, i.e., on one mesh index. For

example, σ_{y1} and σ_{y2} to be used in (34) depends on J. In edge and corner layers, the variation of the conductivity is set equal to that in the adjacent side layer, with the consequence that the conductivities in the PML layer depend only on one mesh index, $\sigma_x = \sigma_x(i)$, $\sigma_y = \sigma_y(j)$, and $\sigma_z = \sigma_z(k)$. As an illustration, at any point located on the right of the plane $J = J_{L2}$ in Fig. 3, we have $\sigma_{y2}(i + \frac{1}{2}, j, k) = \sigma_{y2}(j)$.

From a theoretical point of view, an implementation of variable conductivities does not modify the properties of the absorbing layer since a layer with increasing conductivity can be regarded as a juxtaposition of one-cell thick layers separated by internal interfaces. In side layers, only the longitudinal conductivity vary from one one-cell layer to the next, the transverse conductivities are unchanged (equal to zero). So, there is no reflection from internal interfaces between two adjacent one-cell layers. Similarly, with the implementation described above, there is no reflection from internal interfaces located inside edge and corner layers; in all cases the transverse conductivities do not vary through these interfaces. Considering, for instance, an internal interface normal to z inside a corner layer, σ_z vary through this interface, but the transverse conductivities σ_x and σ_y are identical on both sides of it, since they do not depend on z.

In all the media of Fig. 3, theoretically there are 12 subcomponents. In practice, the number of quantities to be computed is less. In side layers, since the transverse conductivities are equal, there are only 10 quantities to be computed, four subcomponents merging into two usual components. Considering, for example, the right-side layer of Fig. 3, since $\sigma_x = \sigma_z = 0$ and only $E_{yz} + E_{yx}$ is required in (1.h) and (1.k), Eqs. (1.c) and (1.d) merge so that the usual E_y component can replace E_{yz} and E_{yx}. Similarly, due to $\sigma_x^* = \sigma_z^*$, (1.i) and (1.j) merge, so that H_y can replace H_{yz} and H_{yx}. In the edge layers, four subcomponents could also merge into two components, if some conductivities were equal, for example, if $\sigma_{y2} = \sigma_{z2}$ and $\sigma_{y2}^* = \sigma_{z2}^*$ in the x-directed edge of Fig. 3. In practice, the conductivity varies in the layer and such conditions are not satisfied. Similarly, in the corner layers, if all the electric and magnetic conductivities are equal, the medium becomes the classical matched medium involving the six usual components. In practice, due to the variations of the conductivities the 12 subcomponents must be computed separately. In conclusion, in side layers there are only 10 quantities to be computed, and elsewhere 12 quantities. Since most of the PML cells are in side layers, the memory requirements of one PML cell can be roughly estimated to about $\frac{5}{3}$ that of one cell of vacuum.

In the absorbing layers, the magnitude of a plane wave is ruled by the three absorbing terms of (13). In side layers, two absorbing terms equal unity, so that the magnitude is governed by only one exponential term, as in the 2D case [1]. So, for a wave crossing the layer and reflected by the perfectly conducting conditions set on its outer boundary, the apparent reflection is equal to that of the 2D layer. This is in agreement with the fact that the side layers are 2D layers, as remarked above. From [1], for a layer of thickness δ and longitudinal conductivity $\sigma(\rho)$, depending on the distance ρ from the interface, the apparent reflection is, as a function of the angle of incidence θ:

$$R(\theta) = [R(0)]^{\cos\theta} \tag{35}$$

$$R(0) = \exp\left[-\frac{2}{\varepsilon_0 c}\int_0^{\delta}\sigma(\rho)\,d\rho\right]. \tag{36}$$

In this paper, some numerical tests will be shown for various profiles of conductivity, parabolic conductivities as in [1], or conductivities increasing geometrically as in [4], this last profile being an optimum one to reduce the numerical reflection in wave–structure interaction problems. Details on the exact implementation of the conductivity at the mesh points can be found in [1, 4].

3. NUMERICAL EXPERIMENTS

Although based on the use of an absorbing layer designed to remove reflection from the vacuum–layer interfaces, the PML technique is not a perfect method of free-space simulation for two reasons. First, the theoretical reflection of a plane wave is not equal to zero, due to the need of a truncation condition on the outer boundary of

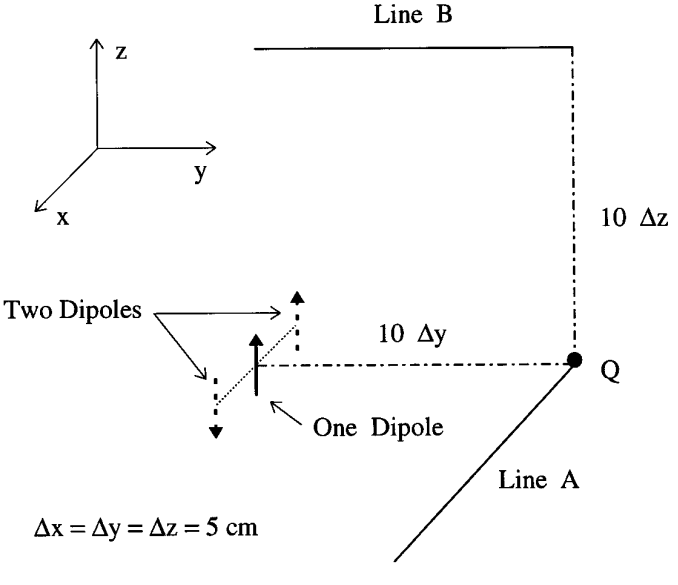

FIG. 4. One or two dipoles radiating in free space. Locations of point Q, line A, line B.

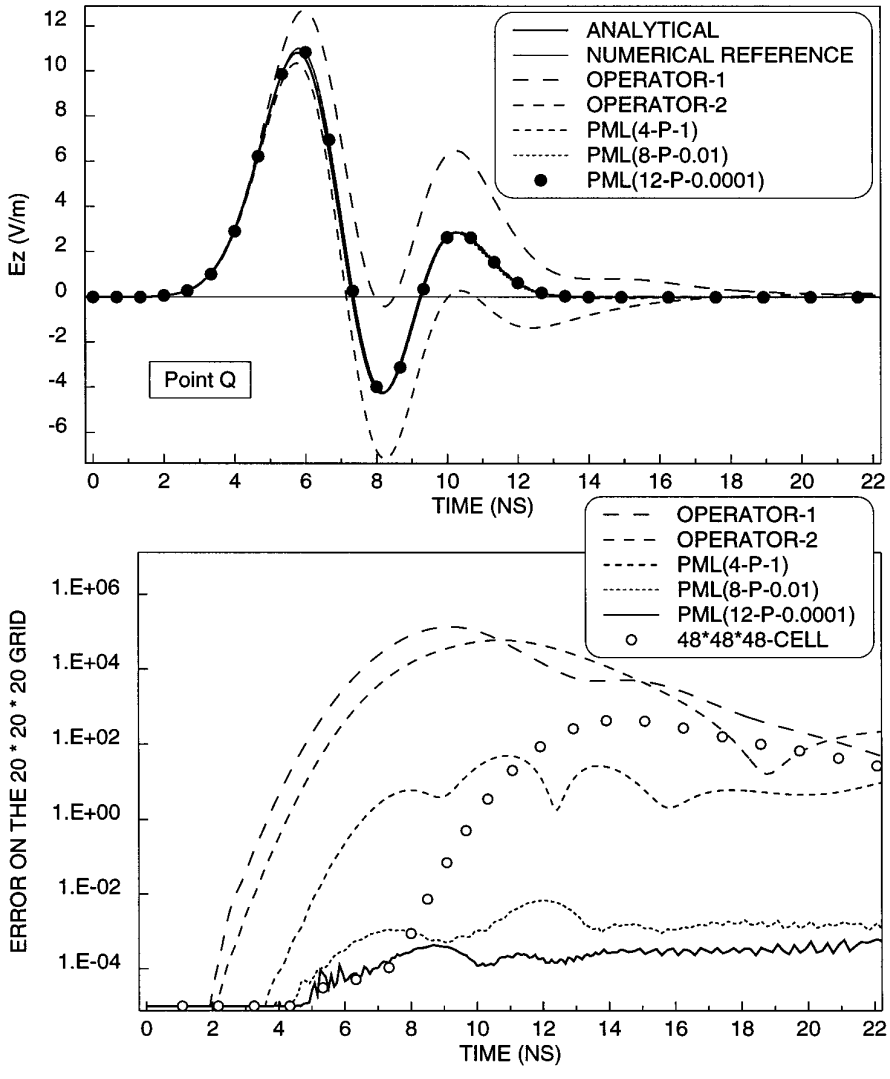

FIG. 5. One dipole located at the center of a 24 * 24 * 24-cell computational domain surrounded by various absorbing boundary conditions. Upper part shows the electric field at point Q. Lower part shows the L^2 error on the 20 * 20 * 20-cell grid surrounding the dipole. The last result in lower part has been computed within a 48 * 48 * 48-cell domain surrounded by the second-order operator.

the layer. With a perfect conductor as truncation condition, the reflection coefficient is given by (35) which equals one at grazing incidence. Second, the discretization of the PML equations results in the presence of numerical dispersion and numerical reflection from the vacuum–layer interfaces. Thus, as in [1] some numerical experiments are presented here in order to evaluate the actual possibilities of the PML technique in practical computations. Most tests of [1] cannot be performed in 3D since their costs would be prohibitive, especially the tests involving a plane wave. We show two tests. The first is related to the absorption of the field radiated by either one or two dipoles. The second is a wave–structure interaction problem. For both, the results computed using the PML technique are compared to the results obtained by other methods of free-space simulation, the matched layer [5, 6] and the first two orders of the Higdon operator given in [1]. This operator is a special case of the general operator described in [7]. Its first order is equivalent to the first order of the one-way approximation of the wave equation [8].

3.1. Radiating Dipoles

We have first considered a computational domain of 24 by 24 by 24 cells of vacuum, surrounded by either a PML layer or an absorbing operator. The sizes of the cell were 5 by 5 by 5 cm and the time step was 83.333 ps. A vertical dipole was located near the center of the domain, at E_z

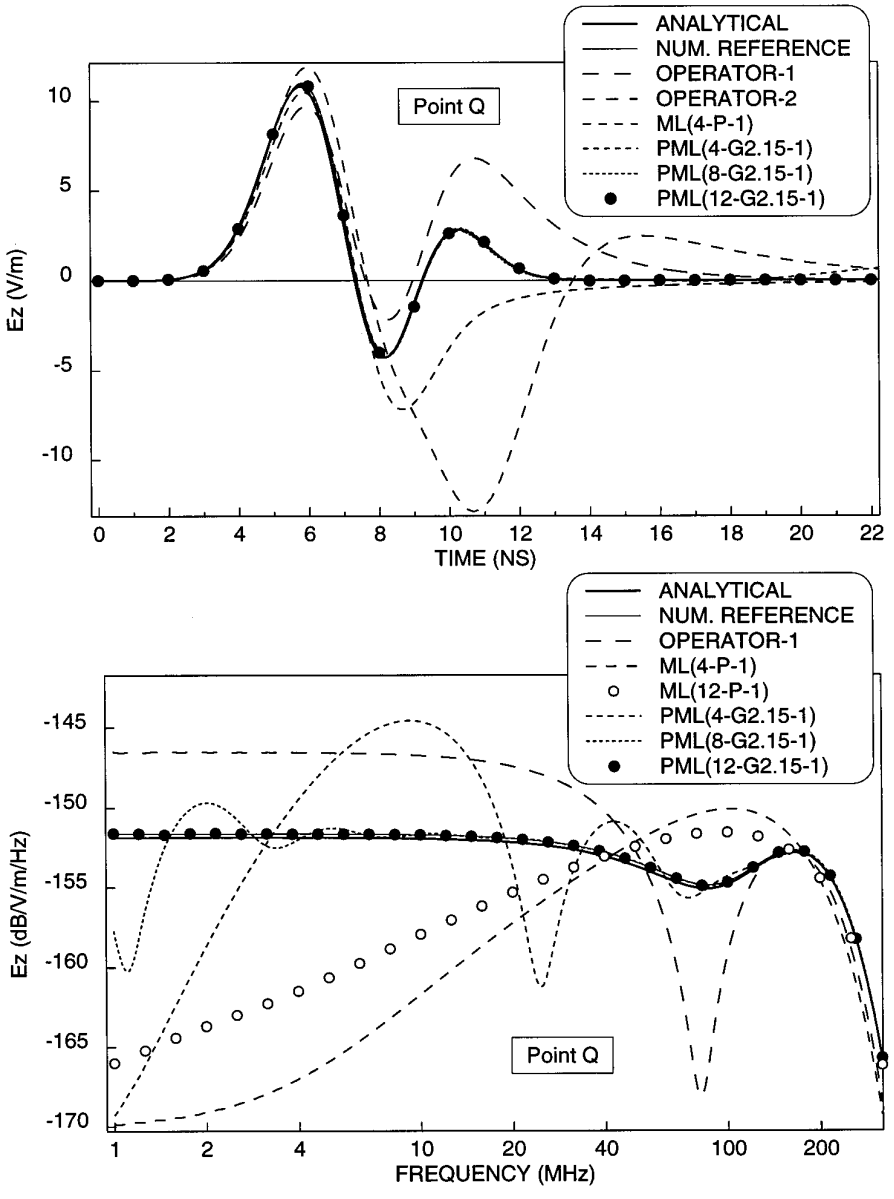

FIG. 6. One dipole located two cells from the corner of a 14 * 14 * 14-cell computational domain. The electric field at point Q is shown in the time domain (upper part) and in the frequency domain (lower part).

point (12, 12, 12 + $\frac{1}{2}$). The electric dipole P_e was implemented by the FDTD equation

$$E_z^{n+1} = E_z^n + \frac{\Delta t}{\varepsilon_0}[\text{curl } H]^{n+1/2} - \frac{\Delta t}{\varepsilon_0 \Delta x^3}\frac{dP_e(t_{n+1/2})}{dt}, \quad (37)$$

where Δx is the spatial increment. The results in this paper were computed using the gaussian pulse,

$$P_e(t) = 10^{-10}\exp\left(-\left(\frac{t-3T}{T}\right)^2\right) \quad (T = 2\,\text{ns}). \quad (38)$$

Beside the computations performed using the boundary conditions to be tested, we computed a reference solution within a domain of 150 by 150 by 150 cells, allowing a boundary-free solution for more than 250 time steps in its center part.

Two kinds of results are reported in Fig. 5. The upper part shows the vertical field E_z at point $Q(12, 22, 12 + \frac{1}{2})$, located 10 cells from the dipole (Fig. 4) and two cells from the absorbing boundary of the 24 * 24 * 24 domain. The results computed using the two operators and three PML layers are compared to the reference solution and

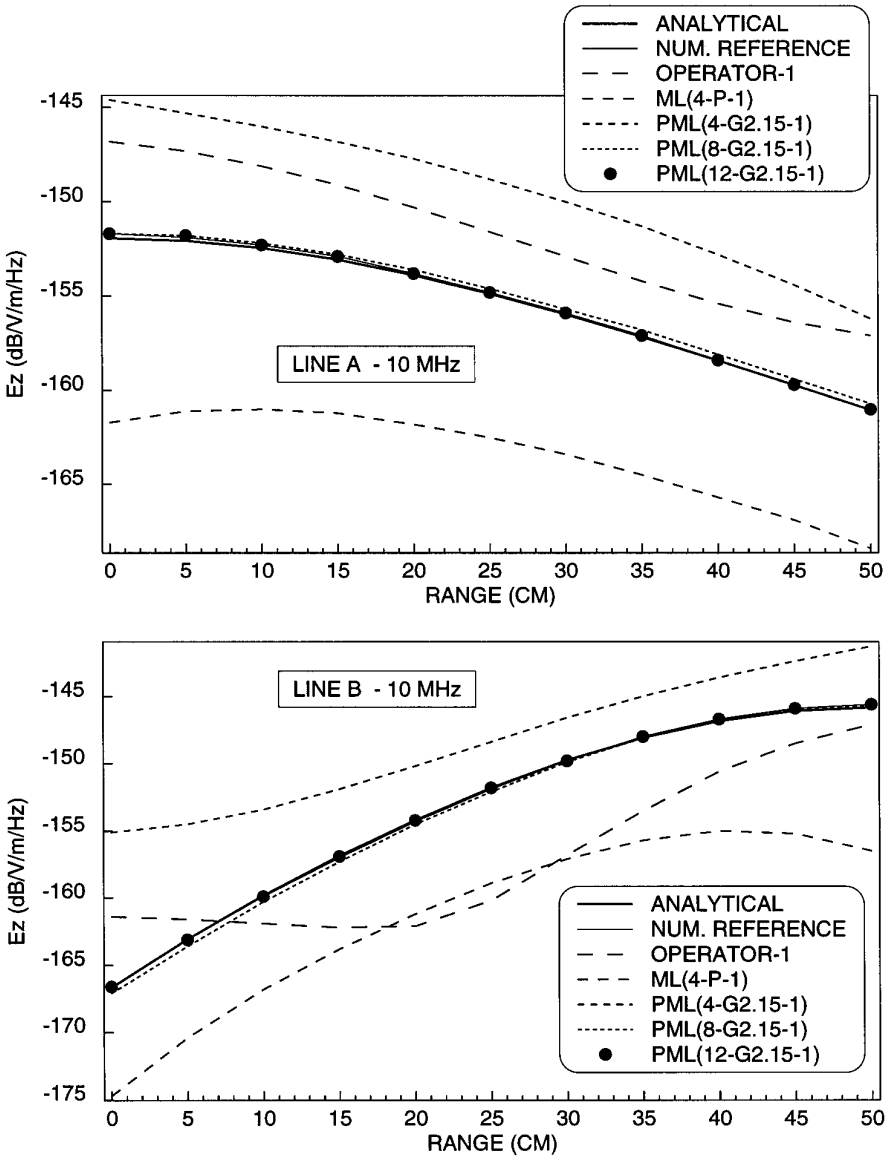

FIG. 7. One dipole located two cells from the corner of a 14 * 14 * 14-cell computational domain. The electric field is shown along lines *A* and *B*, at frequency 10 MHz.

to the analytical solution of the problem. The PML layers are denoted as in [1], for example, a PML(8-P-0.01) layer is a layer of eight cells, a parabolic profile of conductivity, and a normal reflection $R(0)$ equal to 0.01%. As it appears in Fig. 5, the operator method cannot allow an exact solution to be computed. Conversely, using the PML method the results are in very good agreement with the analytical solution and are superimposed on the boundary-free reference.

The lower part of Fig. 5 gives the L^2 norm of the error on the 20 * 20 * 20 grid surrounding the dipole. Denoting as $E_z(i, j, k)$ the field in the test domain and $E_{zr}(i, j, k)$ its counterpart in the reference domain, the quantity reported in Fig. 5 is

$$L^2 = \sum_{i=2}^{22} \sum_{j=2}^{22} \sum_{k=2+1/2}^{21+1/2} [E_z(i, j, k) - E_{zr}(i, j, k)]^2. \quad (39)$$

Figure 5 shows five results computed within the 24 * 24 * 24-cell domain, plus an additional result computed with the dipole at the center of a domain of 48 * 48 * 48 cells surrounded by the second-order operator. These results show that the absorption of the field radiated by the dipole

is widely improved by using the PML method. Comparing to the operator method, the 8-cell and 12-cell PML layers allow the peak of the error to be reduced by more than 10^7. Such a reduction could not be achieved by increasing the computational domain surrounded by an operator, as shown by the case of the $48 * 48 * 48$-cell domain whose computational cost was greater than that of the 8-cell PML case. The results in Fig. 5 are in agreement with those observed in the 2D case [1].

The results in Figs. 6 and 7 were computed within a vacuum reduced to $14 * 14 * 14$ cells, with the dipole located only two cells from a corner, at point $(2, 2, 2 + \frac{1}{2})$. The upper part of Fig. 6 shows the field observed at point Q of Fig. 4, located at $(2, 12, 2 + \frac{1}{2})$ in the reduced grid. Due to the reduction of the domain, with the operator technique the results are worse than those of Fig. 5. Another result was computed using a 4-cell thick matched layer ML(4-P-1), with a parabolic profile of conductivity and a normal reflection of 1%. This result is also in error. Conversely, by using PML layers the results are very good, at least for the 22 ns shown in Fig. 6. In the three PML layers, the conductivity increases as a geometric progression. As a function of the distance from the interface, it is given by

$$\sigma(\rho) = -\frac{\varepsilon_0 c}{2\,\Delta x}\frac{\ln g}{g^N - 1}\ln R(0)\, g^{\rho/\Delta x}, \tag{40}$$

where g is the ratio of the geometric progression, Δx is

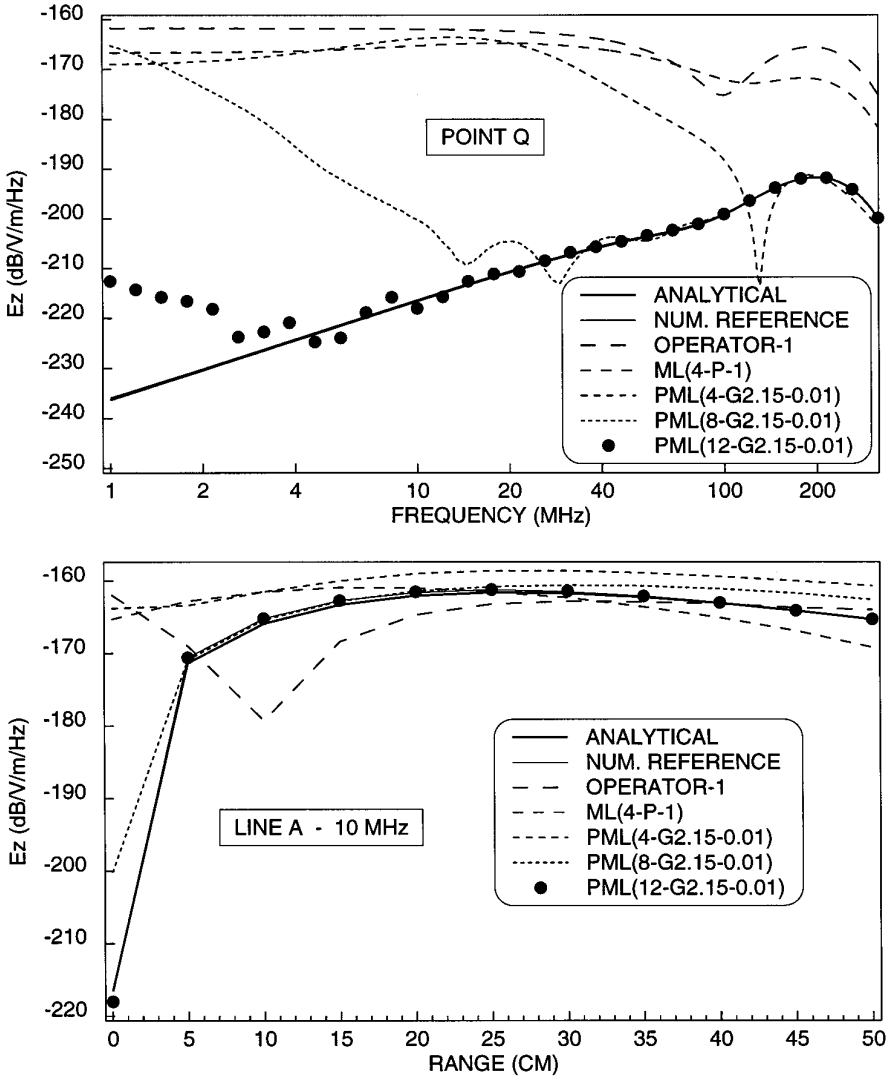

FIG. 8. Two dipoles located near a corner of a $16 * 14 * 14$-cell computational domain. Upper part shows the electric field at point Q in the frequency domain. Lower part shows the electric field along line A, at frequency 10 MHz.

the spatial increment, and N is the number of cells in the layer. Such layers are denoted as PML(N-Gg-$R(0)$).

The lower part of Fig. 6 shows the field at point Q in the frequency domain. To obtain this result we computed the field up to 5000 ns and then performed a Fourier transform. Only the first-order operator is shown in this figure, the second-order one has been found unstable after thousands of time steps. Two results related to the matched layer method are shown, the first one computed with the above 4-cell ML layer and the second one with a thicker 12-cell ML layer. The Fourier transform of the reference has been computed using a 22-ns boundary-free result and supposing that the field equals zero later than 22 ns. As expected, the results computed by the operator and ML techniques differ from the reference at any frequency. Results from the 4-cell and 12-cell ML layers are not quite different. This is due to the fact that the reflection is mainly determined by the physical reflection from the vacuum-ML interface [1, 6]. With PML layers, the results are widely improved. They are superimposed on the reference above a frequency which decreases as the thickness of the layer increases, about 100 MHz with the 4-cell layer and 5 MHz with the 8-cell layer. Such results can be explained by following the way of [4]. In wave–structure interaction problems, it has been found that the domain of validity of the PML technique is bounded by a frequency f_c which depends on the numerical conductivity implemented in the first row of the layer, denoted as $\sigma_n(0)$. From [4],

$$f_c = \frac{\sigma_n(0)}{2\pi\varepsilon_0} = \frac{c}{4\pi\,\Delta x}\frac{1-\sqrt{g}}{g^N-1}\ln R(0). \tag{41}$$

The f_c frequencies of the three layers of Fig. 6 are respectively equal to 50.3, 2.25, and 0.105 MHz. Such frequencies are in accordance with the results in Fig. 6. Thus, Fig. 6 suggests that the analysis of [4] is also valid for radiating antenna problems. One might think that specifications of an optimized PML layer could be determined for antenna problems, as has been done for interaction problems in [4].

Figure 7 shows the magnitude of the E_z component along lines A and B (Fig. 4) located two cells from the absorbing boundary conditions, at frequency 10 MHz. As the operator and ML techniques, the 4-cell PML layer does not allow correct results to be computed since 10 MHz is far below frequency f_c. Conversely, with the 8-cell PML layer the results are close to the reference and with the 12-cell one they are exact.

The results in Fig. 8 were computed within a 16 * 14 * 14-cell domain with a couple of dipoles (Fig. 4) separated by four cells (20 cm), located near a corner, at points (2, 2, 2 + $\frac{1}{2}$) and (6, 2, 2 + $\frac{1}{2}$). The radiated fields were approximately of opposite signs. With P_e from (38), the dipoles were

$$P_{e1}(t) = P_e(t), \quad P_{e2}(t) = -P_e(t+\delta t), \tag{42}$$

where δt is an interval of time. If $\delta t = 0$, then $E_z = 0$ in the plane of antisymmetry ($I = 4$). By an adequate choice of δt, E_z may be small in this plane, at frequencies of interest. The results in Fig. 8 were computed with $\delta t = 0.01$ ns. The upper part gives the field at point Q (4, 12, 2 + $\frac{1}{2}$) and the lower part gives the field along line A, at 10 MHz. We observe that the results are far from the reference when using the operator or ML techniques. With the 8-cell and 12-cell PML layers, the results at point Q are correct above frequencies of 50 MHz and 5 MHz. With the 12-cell layer the 50 dB range of E_z along line A is correctly computed at 10 MHz. Such a test illustrates the very good absorption of the radiated field by PML layers whose normal reflections $R(0)$ were equal to 0.01%.

In conclusion to these experiments with radiating dipoles, reflection from the outer boundary can be widely reduced by using a PML layer in place of the matched layer [5, 6] or the one-way operator [7]. Such an achievement reduces the numerical noise in the FDTD computational domain, resulting in a substantial increase of the dynamic range of the computed results. The computational requirements of PML layers are greater than those of the other methods, due to their thickness and the 10 or 12 subcomponents per cell. But this does not mean that the PML method is less efficient, since such layers allow far better results to be computed within a given computational domain. When comparable accuracies are considered, the other boundary conditions require far greater domains, so that the PML method is more efficient in terms of overall computational requirements. This is illustrated by the 48 * 48 * 48-cell-domain calculation in Fig. 5 whose memory and time requirements were about 2.5 times greater than those of the 24 * 24 * 24-cell domain surrounded by the 4-cell PML layer.

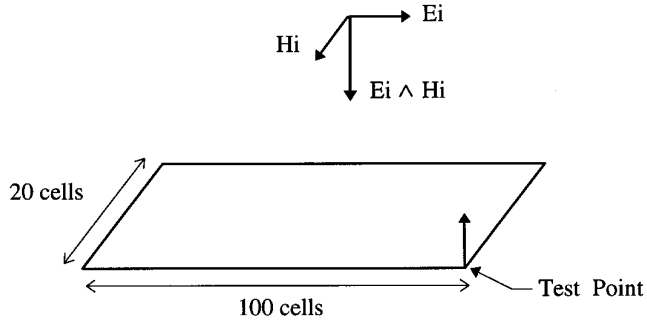

FIG. 9. The 100 * 20-cell plate and the incident wave.

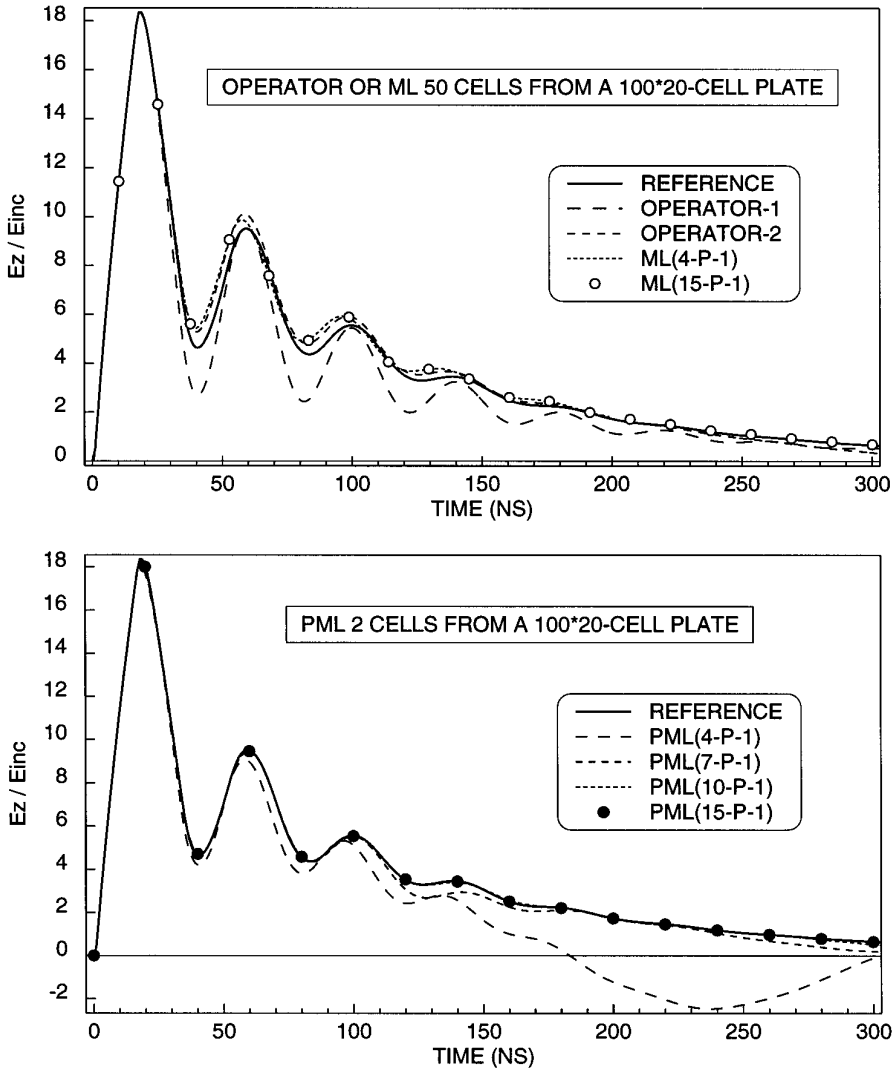

FIG. 10. Wave–structure interaction problem. Electric field at the corner of a 100 * 20-cell plate computed using a matched layer or an operator positioned 50 cells from the plate (upper part), or a parabolic PML layer positioned only two cells from the plate (lower part).

3.2. Wave–Structure Interaction

We have considered the scattering problem of Fig. 9. The scatterer was a plate of 100 by 20 cells and zero thickness. The size of the cubic cell was 5 cm and the incident plane wave propagating downward was

$$E(t) = E_{\text{inc}}(e^{-t/100} - e^{-t}) \quad (t \text{ in nanoseconds}) \quad (43)$$

This problem is close to the 2D test presented in [1]. Figure 10 shows the vertical field at the corner of the plate (Fig. 9). In the upper part, results computed using the matched layer and operator methods are compared to a boundary-free reference solution. The plate was within a 200 * 120 * 100-cell domain of vacuum, so that the absorbing boundaries were 50 cells from the scatterer. The results computed with the 4-cell and 12-cell ML layers are about identical and very close to the result obtained by means of the second-order operator. All the results are only approximate solutions. To obtain better results a larger domain would be required with scatterer-boundary separation at least equal to the size of the scatterer. The lower part of the figure shows the results computed using PML layers set only two cells from the plate, which was then within a 104 * 24 * 4-cell vacuum. The layers are the same as those of [1], with parabolic profiles of conductivity and 4, 7, 10, and 15 cells. The results are like those of the 2D case. Using the 10-cell layer the solution is very close to the reference for the 300 ns in Fig. 10; using the 15-cell layer the result is superimposed on the reference. Thus, as the 2D

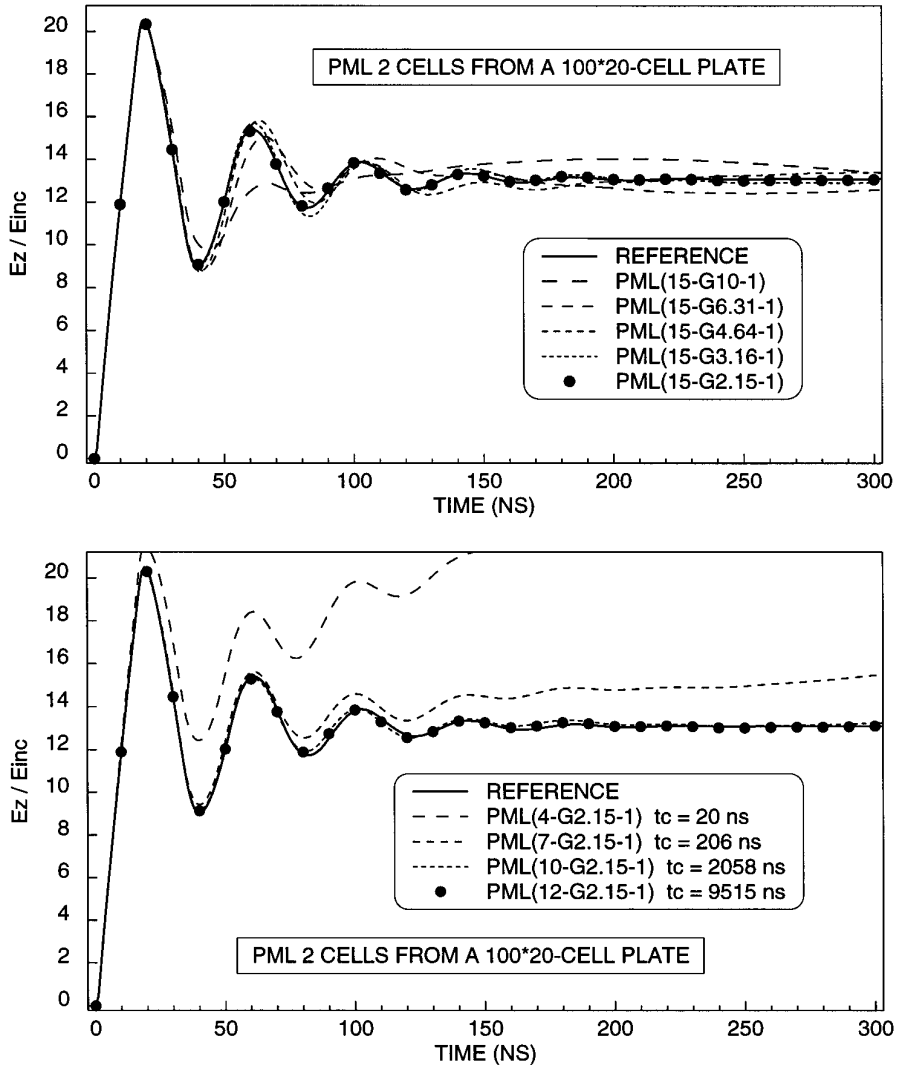

FIG. 11. Wave–structure interaction problem. Electric field at the corner of a 100 * 20-cell plate computed using geometrical PML layers. Upper part illustrates the effect of varying the ratio of the geometric progression. Lower part illustrates the effect of varying the number of cells in the layer.

PML layer, the 3D one allows a very accurate simulation of free space using only a very small vacuum around the scattering structure.

A detailed analysis of wave–structure interaction problems is reported in [4] for 2D problems. It has been found that the optimum profile of conductivity is the geometric progression (40), with $R(0)$ on the order of 1%, g evaluated as a function of the number of cells in the scatterer length, and N set in such a way that the following time, t_c, is at least 10 times the duration of the computation D_c:

$$t_c = \frac{1}{f_c} \geq 10\, D_c \tag{44}$$

Figure 11 illustrates the consequences of varying the parameters g and N. In this test, the incident wave was a unit step (the first exponential of (43) replaced by one). The upper part shows some results computed using 15-cell layers of various g (in each case (44) is satisfied). The results are in agreement with [4]. By reducing g the solution tends towards the reference, g equal to 2.15 ensures a correct solution, as with the 2D 100-cell plate in [4]. The second part of Fig. 11 shows some results obtained using PML layers of various N and, then, various $\sigma_n(0)$ in the first row of the PML mesh. The corresponding t_c are reported in the figure. With the 4-cell and 7-cell layers the solution departs from the reference before the respective t_c times, as expected. With the 10-cell layer, (44) is roughly satisfied (D_c =

300 ns), the solution is correct for the whole time reported in the figure. Thus, the results in Fig. 11 show that the conclusions of the analysis [4] are also valid with the 3D PML layer. Parameters g and N defining the layer can be specified as functions of the number of cells in the scatterer and the duration of the computation, as in the 2D case.

The results in Figs. 10 and 11 also show that the PML method allows the computational requirements to be widely reduced. In each computation, estimates of the memory requirement and computational time can be obtained from the number of unknowns. Taking into account that in PML cells there are 10 subcomponents per cell in side layers and 12 in edge and corner layers, with the 10-cell PML the overall number of unknowns was about 1,400,000 instead of more than 14,400,000 with the operator or ML layer located 50 cells from the plate. That yields an estimate of the ratio of the computational requirements greater than 10. In accordance with such prediction, for the 10-cell-PML and operator calculations, in our computer the ratio of computational times was equal to 10.4. Thus, solving the problem in Fig. 10 with the PML method, memory requirement and computational time were more than 10 times shorter. Moreover, the accuracy was better. If the scatterer-boundary separation were equal to 100 cells, in order to improve the solutions of the operator or ML methods, the gain would be greater, on the order of a factor of 50. Thus, very large reductions of computational requirements can be expected from using the PML method in wave–structure interaction problems. A more detailed discussion related to two realistic scatterers can be found in [9].

4. CONCLUSION

In this paper, the absorbing PML medium [1] has been described in the three-dimensional case. We have shown that all the theoretical properties of the 2D medium [1] are also valid in the 3D case, especially the possibility of zero reflection from interfaces lying between media of different conductivities. As a result, at least in theory, an absorbing reflectionless layer can be built on the outer boundaries of a 3D computational domain, as in the 2D case.

As shown by two finite-difference experiments in this paper, despite a small amount of numerical reflection, the actual simulation of free space by the PML method may be far better than that obtained using methods such as the matched layer [5–6] or the one-way operator [7]. In practical applications of the finite-difference time-domain method, two kinds of improvements can be expected. First, a reduction of the computational burden. Such a reduction is very large when dealing with wave–structure interaction problems, as shown in this paper and in [1, 4, 9]. Second, an increase of accuracy and dynamic range inside the computational domain. This last improvement may be very large, too, in radiation problems as those shown in this paper and in [1, 10, 11], or in other applications as that in [12].

Starting from the material in [1], a lot of work has been done by others about the PML method, resulting in various formulations and modifications of the above PML media. These investigations also provide some interpretations of the PML concept or extend its possibilities. Here we mention those we are aware of. In [13], the PML media are described in terms of stretched coordinates. In [14, 15], discussions about the physical meaning of PML media can be found, along with attempts to reduce the PML equations to the Maxwell equations. It is shown that in side media of a computational domain, in which transverse conductivities equal zero, the PML equations are equivalent to the Maxwell equations with an additional active current density. In [16], the PML method is extended to curvilinear coordinates. In [17, 18], evanescent waves are addressed. In theory, such waves are not reflected from vacuum–PML interfaces. Finally, in [19] the PML layer is extended to lossy media, and in [20] a formulation suitable to the finite-element method is presented.

In conclusion, the PML technique is a very efficient method of free-space simulation, as shown here and in other papers referenced above. Nevertheless, due to the numerical reflection, its implementation in the FDTD method is not perfect. For wave–structure interaction problems as those encountered in electromagnetic compatibility, this reflection is analyzed in [4], allowing an optimized layer to be specified. But we think that this work is only a first step toward controlling and reducing the numerical reflection. Other research should be done in the future, in order to improve and optimize the FDTD implementation of the PML method.

REFERENCES

1. J. P. Bérenger, *J. Comput. Phys.* **114,** 185 (1994).
2. K. S. Yee, *IEEE Trans. Antenna. Propag.* **14,** 302 (1966).
3. A. Taflove, *Wave Motion* **10,** 547 (1988).
4. J. P. Bérenger, *IEEE Trans. Antenna. Propag.* **44**(1), 110 (1996).
5. R. Holland and J. W. Williams, *IEEE Trans. Nucl. Sci.* **30,** 4583 (1983).
6. J. P. Bérenger, *in Actes du Colloque CEM, Trégastel, France, 1983* (unpublished).
7. R. L. Higdon, *Math. Comput.* **49,** 65 (1987).
8. B. Engquist and A. Majda, *Math. Comput.* **31,** 629 (1977).
9. J. P. Bérenger, *Ann. of Telecommun.* **51**(1–2), 39 (1996).
10. D. Eclercy, *Rapport de DEA, Université de Limoges, France,* 1994 (unpublished).

11. D. S. Katz, E. T. Thiele, and A. Taflove, *IEEE Microwave Guid. Wave Lett.* **4**(8), 268 (1994).
12. C. E. Reuter, R. M. Joseph, E. T. Thiele, D. S. Katz, and A. Taflove, *IEEE Microwave Guid. Wave Lett.* **4**(10), 344 (1994).
13. W. C. Chew and W. H. Weedon, *Microw. Opt. Technol. Lett.* **7**(13), 599 (1994).
14. R. Mittra and Ü. Pekel, *IEEE Microwave Guid. Wave Lett.* **5**(3), 84 (1995).
15. C. M. Rappaport, *IEEE Microwave Guid. Wave Lett.* **4**(8), 90 (1995).
16. E. A. Navarro, C. Wu, P. Y. Chung, and J. Litva, *Electron. Lett.* **30**(20), 1654 (1994).
17. J. De Moerloose and M. A. Stuchly, *IEEE Microwave Guid. Wave Lett.* **5**(10), 344 (1995).
18. B. Chen, D. G. Fang, and B. H. Zhou, *IEEE Microwave Guid. Wave Lett.* **5**(11), 399 (1995).
19. J. Fang and Z. Wu, *IEEE Microwave Guid. Wave Lett.* **5**(12), 451 (1995).
20. Ü. Pekel and R. Mittra, *Microwave. Optic. Technol. Lett.* **9**(3), 117 (1995).